Microstructure and Properties of Plasma-Nitrided Fe-Based Superalloy Fe-25Ni-15Cr

XIAOLEI XU, ZHIWEI YU, CAIYUN HOU, WEIXIU SONG, and YINGZHU WANG

Fe-based superalloy Fe-25Ni-15Cr was plasma nitrided at a low temperature of 723 K (450 °C). The nitrided layer was characterized by optical microscopy (OPM) and scanning electron microscopy (SEM) and X-ray diffraction (XRD) through stepwise mechanical polishing and transmission electron microscopy (TEM). The results indicated that the double expanded austenite (γ_{N1} and γ_{N2}) was developed on the nitrided surface. Energy-dispersive X-ray spectrum (EDS) revealed that separate expanded austenite layers with distinctly different nitrogen contents occurred: high (18.98 to 11.49 at. pct) in the surface layer and low (5.87 to 5.32 at. pct) in the subsurface. XRD analysis indicated that large lattice expansion and distortion relative to the untreated austenite of an idea face-centered-cubic (fcc) structure occurred on the γ_{N1}, but low expansion and less distortion on the γ_{N2}. No obvious lattice distortion on the γ_{N1} was determined by calculating its electron diffraction pattern (EDP), except for detectable lattice expansion. Inconformity between XRD and EDP results suggested that the high compressive residual stress in the γ_{N1} was mainly responsible for the lattice distortion of the γ_{N1}. TEM indicated that the γ_{N1} layer exhibited the monotonous contrast characteristic of an amorphous phase contrast to some extent, and corresponding EDP showed a strong diffuse scattering effect. It was suggested that the pre-precipitation took place in the γ_{N1} in the form of strongly bonded Cr-N clusters or pairs. Decomposition of the γ_{N1} into CrN and γ occurred at the grain boundaries, and the orientation of both phases remained cubic and cubic relationship, i.e., the planes and the directions with identical Miller indices in both phases were parallel. The nitrided surface was found to have significantly improved wear resistance. Further, the nitrided surface showed no adverse effect in the corrosion resistance but slight improvement in the 3.5 pct NaCl solution.

I. INTRODUCTION

SUPERALLOYS are commonly used in the aerospace and locomotive industries to fabricate turbine disks, blades, and other critical parts of the aero-engine and locomotive turbocharger[1] owing to their good fatigue, creep properties, and corrosion resistance, where they are subjected to high temperature. Nevertheless, the low hardness and poor wear resistance at high temperature have restricted their applications. Therefore, the surface treatments that can improve surface hardness and anti-wear properties while maintaining excellent corrosion resistance have great potential to extend their application field. Plasma nitriding technology has been widely applied to ferrite steels as well as austenite stainless steel. However, a critical disadvantage associated with nitriding alloys with high Cr content is that, due to the precipitation of chromium nitrides in the nitrided layer, the improvements in surface hardness and tribological properties are always accompanied by a significant loss in corrosion resistance for the traditional plasma nitriding process[2–4] (process temperatures above 773 K (500 °C) or a long duration). To overcome this problem, a low-temperature plasma nitriding technique has been developed.[5] A low-temperature plasma nitriding process of Fe-Cr-Ni austenite stainless steels would produce a thin layer of high hardness with excellent corrosion resistance on the steel surface, which is precipitation free and composed of a single phase termed expanded austenite γ_N.[5–8] The γ_N can be described as a supersaturated interstitial solid solution of nitrogen in the expanded and distorted face-centered-cubic (fcc) lattice of γ-Fe. However, its crystallographic structure is still a controversial issue. The γ_N has been variously described as having a tetragonal, or triclinic lattice, an fcc lattice with either a high density of stacking faults or compressive strain, or both.[9,10] Further, the nature of the γ_N has been investigated recently.[11–13] Compared with austenite stainless steel, a

XIAOLEI XU, ZHIWEI YU, CAIYUN HOU, WEIXIU SONG, and YINGZHU WANG are with the Department of Materials Science and Engineering, Dalian Maritime University, P.R. China. Contact email: 1944816400@qq.com

few studies have been reported on the nitrided superalloys, but mostly on the Ni-base superalloys,[12,14–16] which also give such a γ_N phase when subjected to low-temperature plasma nitriding. The nitrided layer on some austenite stainless steels or Ni-base superalloys obtained at low temperature is complex. It is constituted of two or eventually three distinct layers.[7,12,14,17] The X-ray diffraction (XRD) patterns recorded from the expanded austenite layers exhibit two or three sets of distinct expanded austenite reflections (γ_{N1}, γ_{N2}, or γ_{N3}),[12,14,17] shifted to lower diffraction angles compared to the substrate peaks, which are considered generally as austenite containing two different N contents, associating two different metastable fcc nitrogen solutions denoted γ_{N1} and γ_{N2} (γ_{N3}). The conclusion of the presence of two γ_{N1} and γ_{N2} is based on the XRD patterns or two distinct microstructures. In fact, distinct microstructures were uncertainly revealed in the nitrided surface even after the occurrence of two sets of distinct expanded austenite diffraction peaks.[7] Generally, a continuous nitrogen content profile was always formed, and no proof for two separate sublayers with different nitrogen contents was revealed. This seems to be inconsistent with the presence of two separate expanded austenite sublayers with two distinct nitrogen contents. In the recent work, Fonović et al.[12] showed that a double-layer microstructure was distinctly revealed on the nitrided Ni-based Ni-Ti alloy by optical microscopy (OPM), and distinct expanded austenite reflections of γ_{N1} and γ_{N2} were detected by XRD, but no separate expanded austenite sublayers with distinctly different N content profiles occurred. It was suggested that the stress-assisted diffusion was related to the formation of the double layers, but the depth dependence of N content in the expanded austenite layer did not feature any sublayer-like structure at all.[12] However, some authors have suggested that this enriched nitrogen sublayer was formed during the slow cooling of the substrate after nitriding.[7] In the present work, the double expanded austenite was produced on the nitrided Fe-based superalloy Fe-25Ni-15Cr. Extensive microstructural examinations on the nitrided layer were carried out by step-removal XRD, OPM, scanning electron microscopy (SEM), energy-dispersive X-ray spectrum (EDS), and transmission electron microscopy (TEM). The tribological behavior and corrosion resistance of untreated and nitrided Fe-based superalloy Fe-25Ni-15Cr were evaluated comparatively.

II. EXPERIMENT DETAILS

The material used in the present work was Fe-based superalloy Fe-25Ni-15Cr with the chemical composition (wt pct) C0.06, Si0.66, Mn1.35, Cr15.6, Ni24.71, Al0.31, Mo1.30, Ti2.19, Al0.13, V0.35, and Fe bal. The samples for plasma nitriding were machined into discs of 20-mm diameter and 5-mm thickness. The samples were then ground using SiC grinding paper down to 1500 grade and polished with diamond paste (mean size 1 μm) before nitriding. Plasma nitriding was carried out using a DC plasma nitriding unit (50 kW) at 723 K (450 °C)

for 8 hours in a gas of NH_4 at a pressure of 800 to 930 Pa.

The phases present in the nitrided layer were determined by XRD on a Rigaku D/Max-Ultima diffractometer in symmetric Bragg–Brentanno geometry with Cu K_α radiation ($\lambda = 0.154$ nm). To assess the variation of phase composition with depth in the nitrided layer, XRD profiling was also carried out on the nitrided sample. The sequential removal of 4 to 5 μm from the treated surface was conducted by stepwise mechanical fine polishing. Metallographic specimens were chemically etched in a solution of $FeCl_3$ (5 g) + HCl (5 mL) + water (100 mL). Morphological observations were carried out on a Philips XL-30 scanning electron microscope and an Olympus GX51 optical microscope. The microchemical composition profile in the layer was evaluated by EDS. Additional microstructure analysis was performed on a JEM 2100 transmission electron microscope at a voltage of 200 kV. The specimens for TEM were prepared by grinding and mechanical polishing from the untreated side to about 50 μm, and then TEM disks 3 mm in diameter were punched from it, followed by jet electropolishing from the untreated side to obtain the thin foil of the top layer. It should be mentioned that the plastic film was covered on the treated side of the TEM disk to protect the treated side from the electrolyte during electropolishing. Jet electropolishing was performed on a Struers Tenupol 3 device, using a 10 pct perchloric acid–alcohol solution at a temperature of 253 K (–20 °C) with a polishing current of 80 mA.

The microhardness of the nitrided superalloy was evaluated with a Vickers indenter under various loads. The tribological behaviors of the nitrided and untreated superalloys were determined with a pin-on-disc wear test on a SFT-2M tribometer. The pin of the quenched AISI 52100 steel ball with a diameter of 5 mm was used against the disc. The wear tests were carried out under a load of 5 and 10 N, respectively, without lubrication. An average sliding velocity of 50 mm s^{-1} was used for a distance of 90 m. The coefficient of friction was measured continuously during the tests and recorded on a dedicated, data-acquisition computer. The surface wear morphology was observed by SEM.

The corrosion behavior was evaluated by recording polarization curves in 3.5 pct NaCl solution using a CHI660D electrochemical working station, and the tests were carried out at room temperature. A three-electrode system consists of the specimen as the working electrode, a saturated calomel electrode (SCE) as the reference electrode, and a platinum sheet as the counter electrode. The scan potential was in the range of –800 to 2000 mV (vs SCE), and the scan rate was 1 mV/s.

III. RESULTS AND DISCUSSION

A. SEM and OPM Observation on Cross-Sectional Microstructure

The typical cross-sectional OPM and SEM micrographs of the nitrided sample are shown in Figure 1. It

can be seen that a double-layer microstructure was present. Each layer was relatively homogeneous and distinguished from the other and from the substrate by the etched lines (Figure 1(a)). The metallographic features were observed in nitrided stainless steels and Ni-based Ni-Ti alloy and Ni-based INCONEL*

---

*INCONEL is a trademark of Special Metals Corporation, New Hartford, NY.

690,[14,17,18] which were described as "outer layer" and "inner layer," or denoted as γ_{N1} and γ_{N2}. In the present work, EDS analysis later will demonstrate that the inner layer is also a nitrogen-rich layer. Therefore, the topmost surface layer was denoted as γ_{N1}, and the second layer between the substrate and the top layer γ_{N1} was denoted as γ_{N2} (as seen in Figure 1). The thicknesses of both layers were, respectively, about 20 and 8 μm. Many slip lines concentrated in the γ_{N1} layer, and they extended deeply into the layer. Occasionally, intergranular cracking was observable in the γ_{N1} layer, demonstrating brittleness. It was suggested that solid solution nitrogen in the γ_{N1} layer produced both considerable plastic deformation and high residual internal stresses.[18] However, no slip lines were observed in the γ_{N2} layer, suggesting that the stress level in the γ_{N2} layer was much lower than that in the γ_{N1} layer.

The "featureless" appearance was present in grains of the γ_{N1} layer, except for boundaries and slip lines (Figure 1). However, the austenite grains in the substrate were attacked by the used etchant, showing shallow pits in SEM (Figure 1(b)). Also, no pits were found in the γ_{N2} layer. The phenomena suggested that the pitting occurred on the substrate without the occurrence on the layer. This was a convincing evidence that the nitrided layer showed better corrosion resistance in the used etchant, compared with the untreated substrate. From Figure 1, the grain boundaries were outlined in the layer, and they showed continuation of the substrate austenite grain boundaries. Some boundary lines even continued from the substrate to the γ_{N2} layer (indicated by arrows in Figure 1(b)), although the austenite grain boundary lines became faint when extending to the layer surface, which was also evidenced by the continuation of substrate austenite grains. It was suggested that the nitriding layer seemed to retain some microstructural characteristics of the substrate. Additionally, the disappearance of the boundary lines in the γ_{N2} layer close to the γ_{N1} layer also demonstrated that the γ_{N2} layer obtained better corrosion resistance due to the nitrogen incorporation in the used etchant.

B. Microcomposition Evaluation

Semiquantitative analysis of elements in the nitrided layer was determined by EDS. The typical concentration-depth profiles of nitrogen and major substitutional alloying elements Cr, Ni, and Fe are shown in Figure 2. It can be seen that N content decreased gradually from
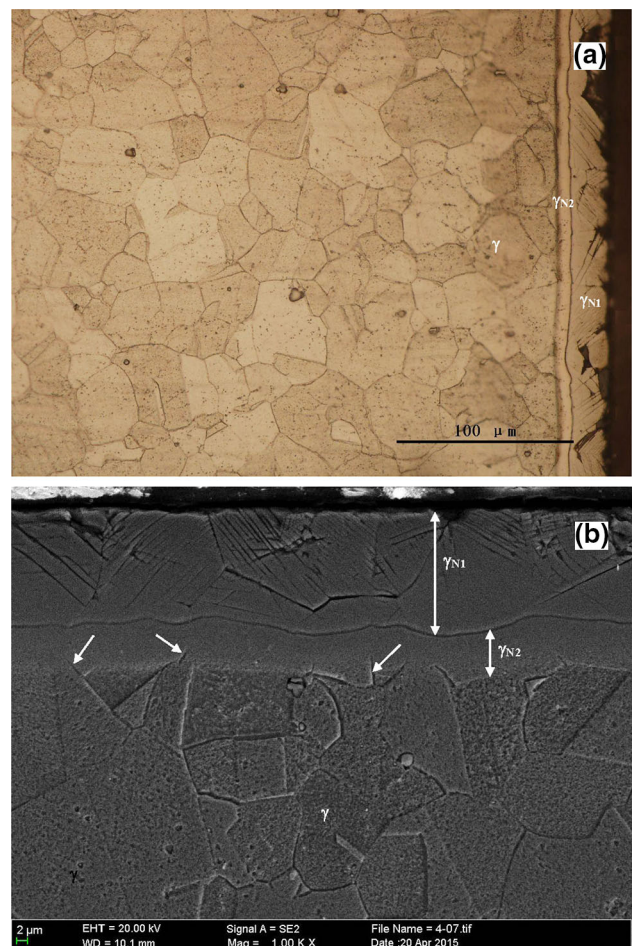

Fig. 1—Cross-sectional micrographs of the nitrided sample: (a) OPM observation and (b) SEM observation.

18.98 to 11.49 at. pct within a depth of 0 to 20 μm, i.e., a depth range of the γ_{N1} layer as revealed by SEM, followed by a significantly decreasing nitrogen content (from 11.49 to 5.87 at. pct), and the nitrogen concentration profile showed an almost constant N content (between 5.87 to 5.32 at. pct) in the depth range from 20 to 28 μm, i.e., a depth range of the γ_{N2} layer. Beyond 29-μm depth, the un-nitrided substrate occurred. It is well known that the maximum solubility of nitrogen in austenite is 10.3 at. pct [923 K (650 °C)].[19] It was concluded that the γ_{N1} layer was mainly composed of the supersaturated solid solution of nitrogen in austenite, and the nitrogen enrichment also took place in the γ_{N2} layer in spite of sharply decreasing nitrogen concentration to a level of 5.32 to 5.87 at. pct, less than the maximum solubility of nitrogen in austenite. It was suggested that a double-layer structure was characterized by high nitrogen content (11.49 to 18.98 at. pct) in the γ_{N1} layer and low nitrogen content (5.32 to 5.87 at. pct) in the γ_{N2} sublayer.

The major substitutional alloying elements Cr, Ni, and Fe have no obvious redistribution throughout the nitrided zone because of their low diffusivity at low nitriding temperature.

C. XRD Results

XRD patterns of the nitrided and untreated samples are shown in Figure 3(a), together with the enlarged pattern of the angles (2θ) from 37 to 55 deg for clarity (Figure 3(b)). The results indicated that the untreated sample was composed of γ-austenite and the peaks were sharp. The peaks of the phase induced by nitriding appeared at the lower 2θ angles than those of the substrate austenite, and all were broadened considerably. The shift of the austenite peaks toward lower diffraction angles was indicative of the lattice expansion due to nitrogen in the interstitial solution, compared with the austenite substrate. Therefore, the broad peaks were associated with a metastable phase termed "expanded austenite," γ_N, or supersaturated nitrogen austenite.[5–10] The austenite reflections from the underlying untreated substrate were not detected, indicating that the information depth of XRD was smaller than the thickness of the nitrided layer.

XRD analysis was conducted by removing successive layers from the nitrided surface, in order to assess the variation in diffraction behavior with depth in the layer. The XRD patterns at various removal depths are shown in Figure 4. The lattice parameters were calculated from $d(111)$ and from $d(200)$ measured by XRD according to $a_{hkl} = d_{hkl} (h^2 + k^2 + l^2)^{1/2}$ assuming an fcc lattice (Figure 5(a)). The relative expansion of the austenite lattice, $\Delta a/a_\gamma$ (pct), against depth is shown in Figure 5(b), where $\Delta a = a_{\gamma N} - a_\gamma$. The peaks of γ_{N1} appeared at lower diffraction angles than the peaks of the substrate austenite at every depth. The gradual peak shift of the γ_{N1} to a higher angle with increasing depth into the nitrided layer was observed. As expected, the lattice parameter of the supersaturated solid solution γ_{N1} decreased gradually with increased removal due to the gradual reduction of nitrogen content. Thus, the measured lattice expansion ($\Delta a/a_\gamma$) of the γ_{N1} decreased gradually with increased removal in a continuous manner (as seen in Figure 5(b)). The effect of further removal was the more apparent reduction in the relative intensities of the γ_{N1} peaks. It was noted that, along with the decrease in the intensity of γ_{N1} peaks, another family

of peaks of weaker intensity with less-expanded fcc structure started to appear with increased removal (at the removal of about 9.5 μm, seen in Figures 4(a) and (b)), which were labeled as γ_{N2} in Figure 4(b), indicating that the information depth of XRD was beyond the remaining thickness of the γ_{N1}. It was suggested that the dual phases were in a double-layer structure with the γ_{N2} underlying the γ_{N1} layer, in agreement with SEM and OPM observations on the nitrided layer. The diffraction peaks of γ_{N2} also shifted gradually toward higher angles with the increased removal (Figure 4), and the lattice parameter decreased gradually to be close to the value for the substrate austenite (Figure 5).

It should be highlighted that a continuous lattice parameter profile did not occur as in the aforementioned work.[12] The lattice parameter of γ_{N1} progressively decreased with depth, but a significant and abrupt reduction in lattice parameter from γ_{N1} to γ_{N2} occurred and the variation of the lattice parameter of γ_{N2} was small within the sublayer. The profile of the lattice parameter in the case layer (Figure 5) was correlated to
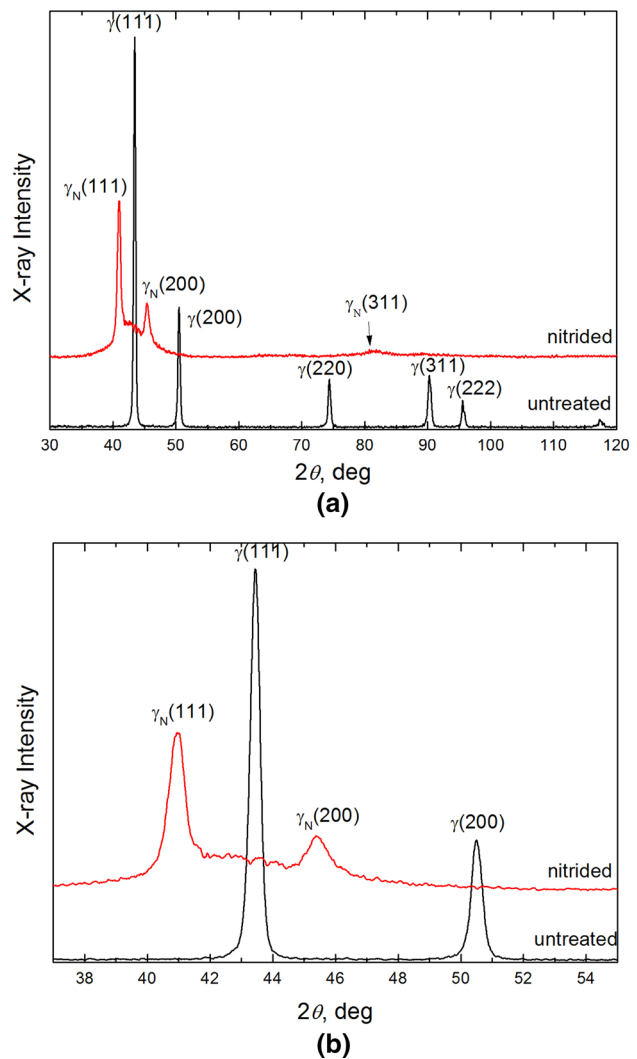
Fig. 3—XRD patterns of untreated and nitrided samples: (*a*) overall pattern and (*b*) enlarged pattern.
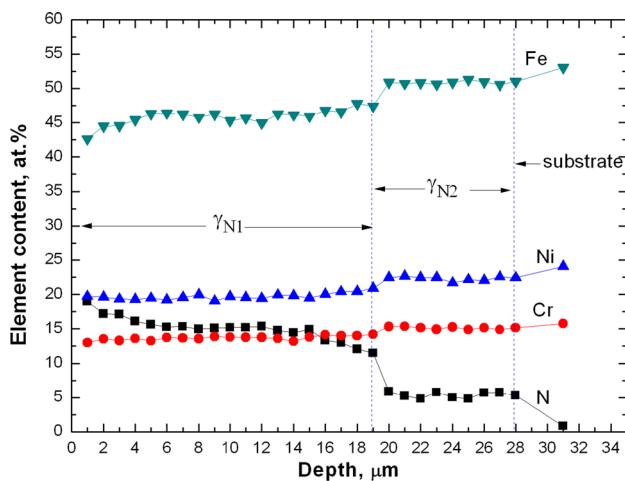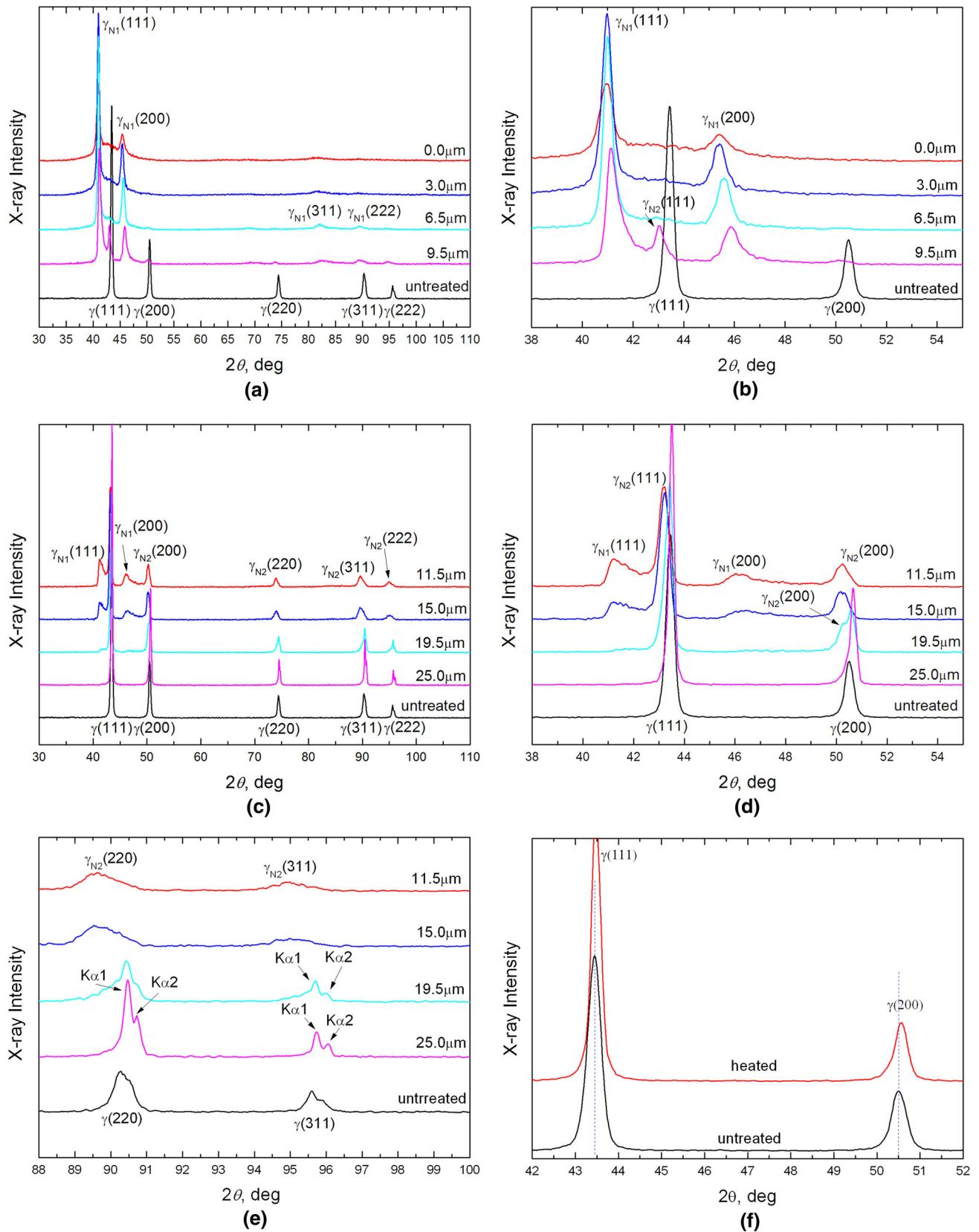
Fig. 2—Composition profiles evaluated by EDS.

Fig. 4—XRD patterns of the nitrided samples in different removal ranges and the heated sample at the nitriding temperature: (*a*) overall patterns (removal 0 to 9.5 μm), (*b*) enlarged patterns of (a) from 2θ of 37 to 55 deg, (*c*) over patterns (removal 11.5 to 25.5 μm), (*d*) enlarged patterns of (c) from 2θ of 37 to 55 deg, (*e*) enlarged patterns of (c) from 2θ of 87 to 100 deg, and (*f*) heated and untreated samples.
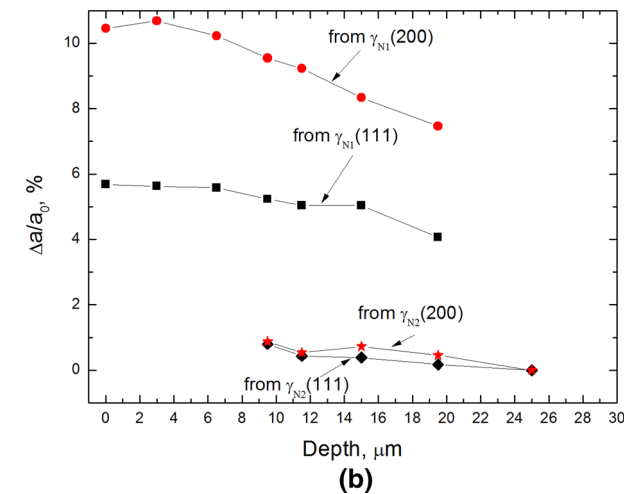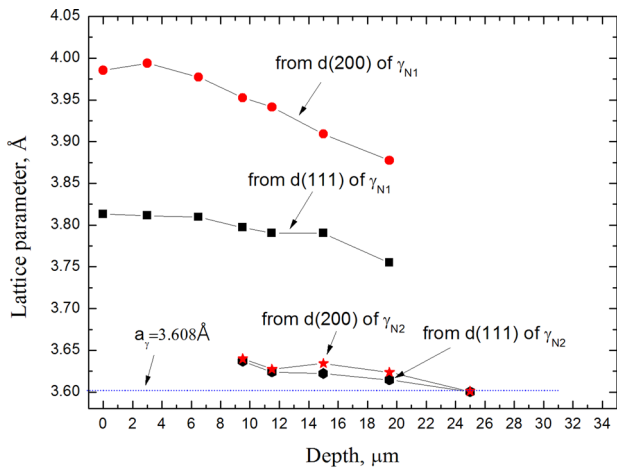
Fig. 6—Lattice distortion-depth profile.

Table I. Elastic Constant and Faults Parameters for Various Reflections[24]

hkl	$(S1)_{hkl} \times 10^5$ (kg/mm^2)	$G_{hkl} \times 10^2$
111	−0.97	−3.45
200	−2.97	+6.89
220	−1.47	−3.45
311	−2.03	+1.25

Note that the (200) peak of the γ_{N1} was shifted more than the (111) peak, relative to the substrate peaks, at every depth. That is, the relative difference in lattice parameter, $\Delta a/a_\gamma$, was larger for the (200) vs the (111) planes at every depth (Figure 5). This indicated that there seemed to be a distortion relative to an ideal fcc lattice. In order to show a picture of the inter-relationship between the degree of distortion and the nitrogen content, the ratio $d(111)/d(200)$, which represents the amount of the distortion, was used as the ordinate for a plot against depth (Figure 6), which represents the nitrogen content at different depths. It is well known that $d(111)/d(200)$ for an ideal fcc structure is 1.155. From Figure 6, it can be seen that the ratio of $d(111)/d(200)$ of γ_{N1} significantly deviated from that of $d(111)/d(200)$ for an ideal fcc lattice. The degree of lattice distortion decreased with depth, or, conversely, increased with nitrogen content. However, it can be seen from Figure 6 that all the data points of $d(111)/d(200)$ for γ_{N2} fluctuated around the ideal value of 1.155, and the slight discrepancy should be considered to be the experimental and instrumental errors. It was suggested that no evident lattice distortion relative to the fcc lattice occurred on the γ_{N2} layer with low nitrogen concentration.

The possible mechanisms of the anomalous expansion reported in the literature in view of the observed XRD diffraction results focus on the following several points.

1. The variation in the nitrogen content is related to the grain orientation.[20] In the present work, no direct evidence of deeper N diffusion in the (200)

Fig. 5—Lattice parameter and lattice expansion depth profiles from XRD peaks of (111) and (200) planes: (a) lattice parameter-depth profile and (b) lattice expansion-depth profile.

the profile of the nitrogen content in the case layer by EDS (Figure 2). This suggested that there were two separate expanded austenite sublayers of distinctly different nitrogen contents.

Unexpectedly, it was found that the peaks of substrate austenite of the nitrided sample shifted to slightly higher angles relative to the peaks of austenite of the untreated sample (as seen in Figure 4(d), at the removal of 25 μm) indicative of smaller d spacing. This also occurred on the nitrided AISI 316 stainless steel and Ni-based superalloy INCONEL 600, which was attributed to in-plane tensile stress in the substrate by Williamson et al.[17] In order to explore the reason, the sample was heated at the nitriding temperature [723 K (450 °C)]. It was found that the austenite peaks of the heated sample also shifted to slightly higher angles relative to the untreated sample (Figure 4(f)), while the tensile stress could not be induced on the surface of the heated sample. It was suggested that the decrease in d spacing of substrate austenite of the nitrided sample was most likely related to pre-precipitation of specific alloy compounds in substrate due to heating aging in nitriding.
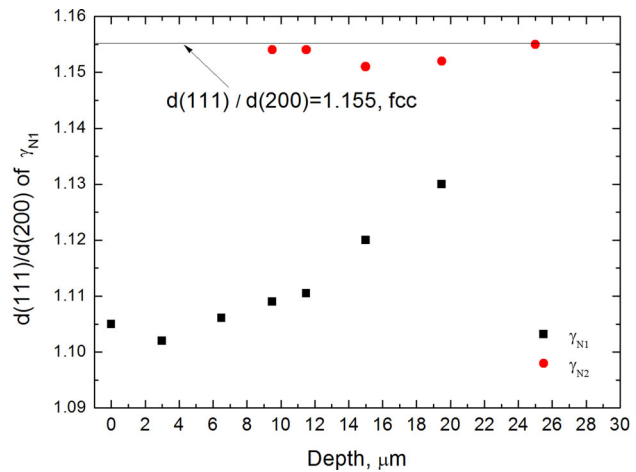
oriented grains than the (111) grains was revealed in view of the almost simultaneous disappearance of (111) and (200) peaks of γ_{N1} at the removal of 19.5 μm.

2. Tetragonal, monoclinic, and triclinic distortion[10,21] are not certain because the corresponding peak splitting was not detected in the present XRD results.

3. Lattice strain resulting from residual macrocompressive stress and a high stacking fault density generated by the interstitial nitrogen have been confirmed by many investigations.[22–26] In the present work, the occurrence of a lot of slip lines in the γ_{N1} layer provided evidence sufficient to support the fact that extremely high residual stress was introduced in the γ_{N1} layer. Obvious plastic deformation in the γ_{N2} layer associated with the high residual stress and, consequently, anomalous expansion in the γ_{N2} were not found. This indirectly confirmed that the higher residual stress in the supersaturated nitrogen solution should be mainly responsible for the anomalous lattice expansion of the γ_{N1}. Residual stresses in the material can result in a shift of the diffraction peak, and the degree of shift depends on the stress level and the elastic constant of the diffraction. Then the change in lattice parameter is given by Eq. [1], as follows.[24]

$$\Delta a_{hkl} = a_0 (S1)_{hkl} \sigma \qquad [1]$$

where $(S1)_{hkl}$ is the elastic constant and σ is the residual stress. Since the crystal structure and elastic properties of the γ_N phase are uncertain, it is impossible to accurately evaluate the $(S1)_{hkl}$ of the γ_N phase. Therefore, the $(S1)_{hkl}$ values for the γ_N phase in the published works varied,[24,27,28] and the $(S1)_{hkl}$ values for an austenitic Fe-Cr-Ni alloy are listed in Table I.[24] From these data, it can be assured that the compressive residual stress in the fcc lattice causes all of the diffraction peaks to shift toward lower angles (i.e., lattice expansion), and the degree of peak shift is larger for the (200) plane than for the (111) plane due to the higher elastic constant in the [200] direction than in the [111] direction. This leads to a lower $d(111)/d(200)$ ratio.

On the other hand, stacking faults can influence not only the profile (peak broadening) but also the position (peak shift).[29,30] Then the change in the lattice parameter is given by Eq. [2][24]:

$$\Delta a_{hkl} = a_0 G_{hkl} \alpha \qquad [2]$$

where α is the stacking fault probability and G_{hkl} is the characteristic parameter of stacking fault (as given in Table I). It can be seen that both the magnitude and the sign of peak shift associated with stacking fault are Miller indice (hkl) dependent. From Table I, the (200) peak is shifted to a lower angle, but the (111) peak shifted to a higher angle to result in a lower $d(111)/d(200)$ ratio. Apparently, the contribution of both faults and compressive stresses would lead to a further decrease in the $d(111)/d(200)$ ratio. However, without obtaining the lattice parameter of the nonstress and
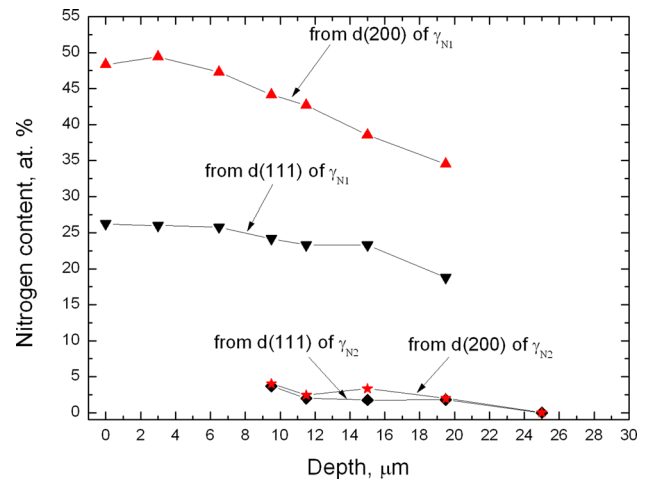

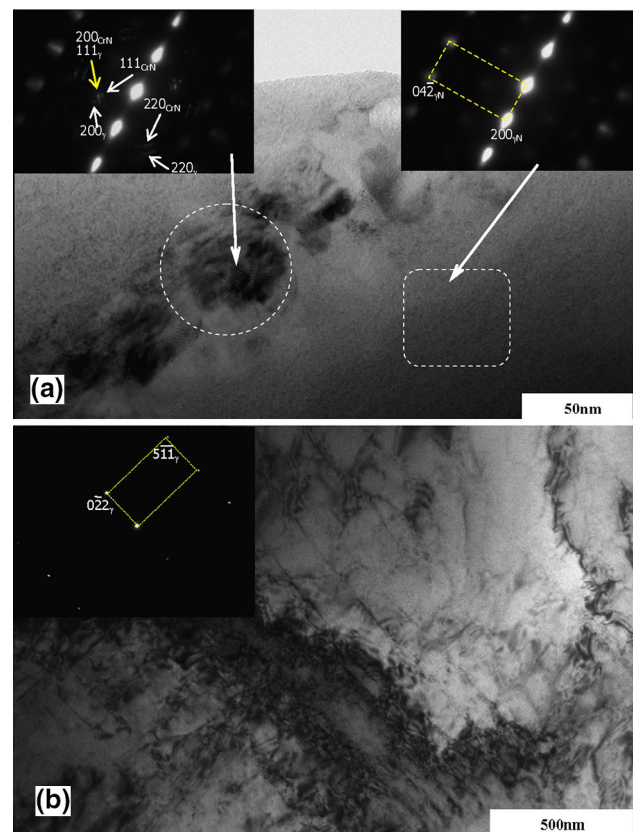Fig. 7—Nitrogen content-depth profile from XRD peaks of (111) and (200) planes.

Fig. 8—TEM observations on the nitrided surface and untreated substrate: (a) nitrided layer and (b) substrate.

nonfault γ_N phases in the layer, it is impossible to accurately evaluate the relative contribution of residual stress and stacking fault to the observed peak shift. Generally, the compressive residual stresses have a stronger effect on the peak shift, and then the residual stresses have been considered as a valid explanation for peak shift. Although metallographic examinations by OPM and SEM did not directly reveal the presence of

stacking faults in the γ_{N1} layer, the formation of slip lines is usually accompanied with the formation of stacking faults. The formation of stacking faults in the γ_{N1} layer is facilitated by the high internal stresses and strains and the supersaturation of nitrogen, which is known to decrease the stacking fault energy in austenite. Therefore, the contribution of stacking faults should be taken into account, although the peak displacement is usually quite small.

It should be mentioned that an intense interaction occurs among the three major influences (supersaturation, stress in the layer, and defect density). The supersaturation causes stresses and the stresses cause defects and *vice versa*, so it is almost impossible to separate individual roles.

Three causes of the broadening of a diffraction peak are now recognized: nonuniform strain due to the gradient of residual microstress, stacking faults, and fine grain or particle size.[29,30] The preceding microstructure showed that the austenite grain size in the layer had no obvious change, compared with the untreated. Therefore, broadening of the peaks was probably caused by the gradient of nitrogen, residual microstress, and the possible defect structure in the nitrided layer. The obvious broadened peaks for γ_{N1} are shown in Figure 4. This was attributed to high residual microstress and stacking faults, which were confirmed by the presence of many slip lines in the γ_{N1} layer. Broadening of the diffraction peaks of the γ_{N2} layer was also detectable, compared with the peaks of untreated substrate. However, the variation in degree of broadening with removal was not evident from the XRD patterns. A slight degree of strain can be detected by observation of the K_α doublet, rather than by attempting to measure a slight increase in line width.[30] The XRD tests on the cold-worked metal or alloy prove that the ratio of the height of the "valley" between $K_{\alpha1}$ and $K_{\alpha1}$ to the height of $K_{\alpha2}$ represents the extent of strain and the ratio increases rapidly as the lines broaden.[30] Seeing (220) and (311) peaks of the γ_{N2} in Figure 4(e), as removal increased, the broadened peaks started to separate into two resolved doublets, one component due to $K_{\alpha1}$ and the other to $K_{\alpha2}$, and the ratio defined previously was decreased. In other words, with the increased nitrogen content, the broadening increased until finally the two components of the doublet overlapped to such an extent that they appeared as one unsolved peak, indicating a gradual increase in magnitude of the residual microstress. An unsolved K_α doublet, therefore, can be taken as evidence of strain.

The atomic nitrogen concentrations (C_N) of γ_N based on the γ_N (111) and γ_N (200) peak positions were calculated according to Picard's equation[20,31,32]:

$$a_{\gamma N} = a_\gamma + kC_N \qquad [3]$$

where $a_{\gamma N}$ and a_γ are the unstrained lattice parameters of the N-rich layer and the substrate, respectively, and k is the Vegard's constant, which is 0.0078 Å at. pct N for pure γ-Fe. The nitrogen concentration profiles with depth based on XRD data and Eq. [3] are shown in Figure 7. It can be seen that the nitrogen concentrations

in the γ_{N1} layer at different depths calculated from the interplanar spacing of the (111) and (200) reflections of γ_{N1} are much higher than the values evaluated by experimental concentration analysis based on EDS (Figure 2). It is suggested that when performing the content-depth profile (XRD N contents *vs* XRD N depths) in the nitrided layer, some correction should be conducted. As described previously, the peak shift by macrostresses should be considered, and stacking faults, inherent to expanded austenite, would also give rise to a systematic lattice parameter deviancy.[9,27] In fact, the actual value of k would become larger when the lattice parameter of γ_N is corrected for the macroscopic stress effect.[27] This means that the nitrogen contents calculated by Picard's equation (Eq. [3]) from the (111) and (200) reflections would be lowered after compensating for the peak shift by macroscopic residual stresses generated by nitridation—more in the (200) planes than the (111) ones, because the (200) planes are affected even more by the stresses. Of course, if there is a nitrogen distribution with depth, then there would be a residual stress profile with depth related to the nitrogen concentration profile. The nitrogen concentration in the γ_{N2} layer predicted from the (111) and (200) reflections of γ_{N2} was found to correlate well with the EDS results. In fact, Eq. [3] is a well-established equation for the lattice parameter of γ-Fe as a function of atomic percent interstitial nitrogen up to ~10 at. pct. Therefore, the estimated nitrogen concentration in the γ_{N2} layer from XRD and Eq. [3] was approximately consistent with the actual nitrogen content evaluated by EDS. In view of no inhomogeneous lattice expansion in the γ_{N2} and consistent N concentration results between the EDS and XRD, it was suggested that the macrostress in the γ_{N2} layer was too small to contribute to the shift of the diffraction peaks. The smaller lattice expansion of the γ_{N2} phase mainly resulted from the interstitial nitrogen in the lattice (less than 10 at. pct).

D. TEM Observation

TEM observation revealed more detailed structural characteristics in the layer surface, γ_{N1} layer. A typical bright-field TEM micrograph of the γ_{N1} is shown in Figure 8, which was comprised of two distinctive microstructures. It can be seen that the grain boundary seemed to be decorated by precipitates, where the expanded austenite had decomposed.

When conducting selected area electron diffraction from a single austenite grain, apparently without precipitates (boxed area in Figure 8), a single crystal pattern was obtained (as seen in the inset on the right) and, importantly, the diffraction spots were diffused in the form of trailing or broadening of the diffraction spots, evidently different from the sharp spots from the untreated austenite (the inset in Figure 8(b)). The diffuse diffraction spots were broad, in just the same way as XRD peaks from this layer tended to be broad. As the region defined by the selected-area aperture was moved around the boundary (circled area in Figure 8(a)), weak discontinuous rings overlapped on a strong diffuse spots pattern (as seen in the inset on the left in Figure 8(a)).
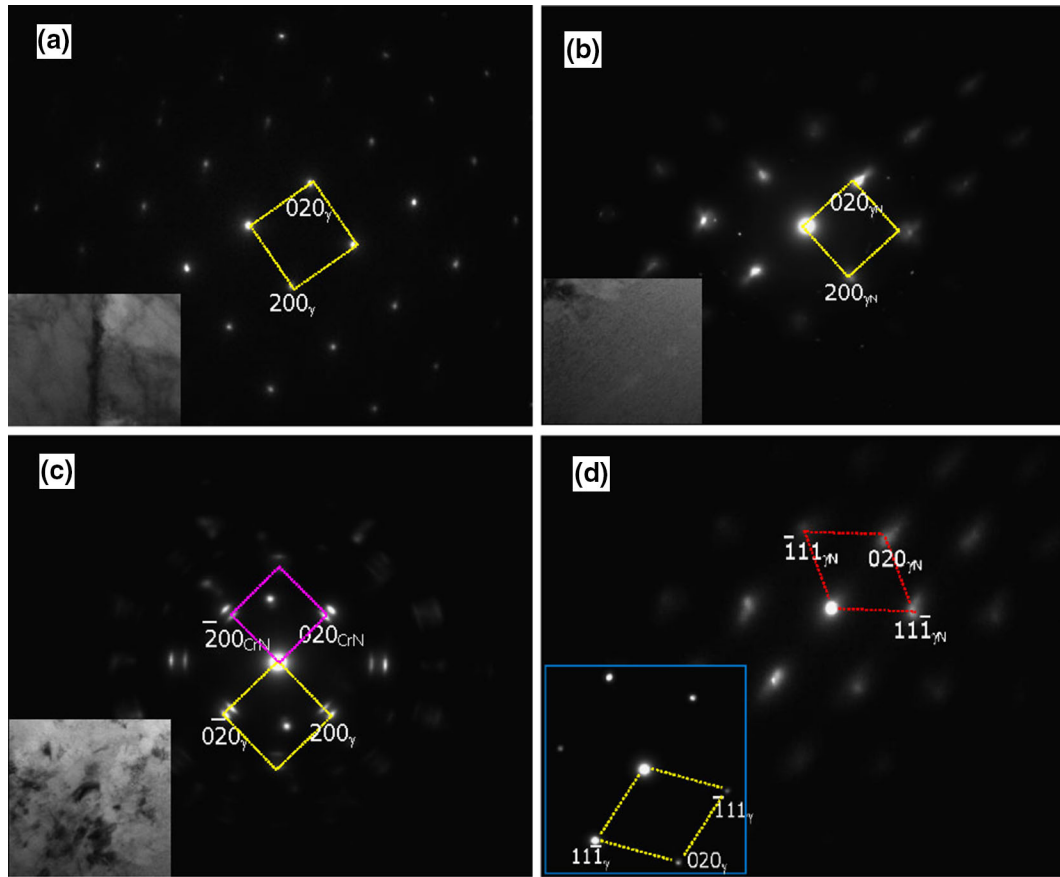
Fig. 9—Selected area electron diffraction pattern of various regions: (*a*) untreated austenite, (*b*) expanded austenite (γ_{N1}), (*c*) decomposition region at the boundary, and (*d*) expanded austenite (γ_{N1}) and untreated austenite (inset).
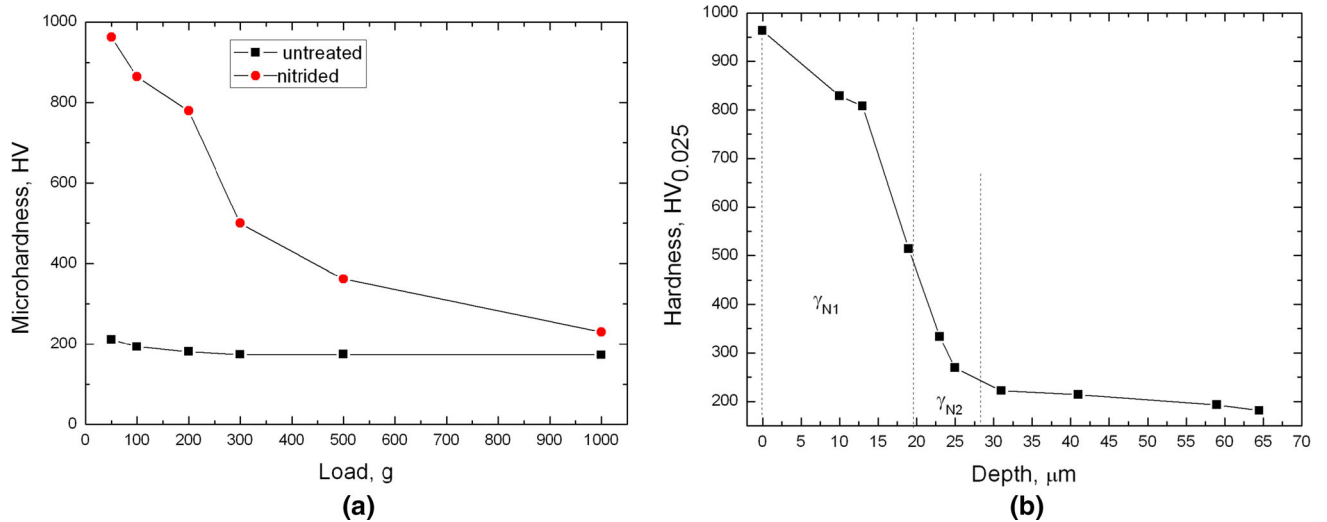

Fig. 10—Hardness results: (*a*) surface hardness and (*b*) hardness profile of the layer.

The diffused diffraction spots were identified as typical of expanded austenite described in the previous literature,[26] which corresponds to the γ_{N1} in the present work. Much debate on the exact nature of expanded austenite is presented in the literature, which mainly comes from XRD data. The expansion along the $\langle 100 \rangle$ direction is larger than that along the $\langle 111 \rangle$ direction. However, attempts to interpret this distortion as triclinic or tetragonal distortion of the lattice have not been confirmed due to the absence of splitting peaks. In order

to further probe the structural nature of the expanded austenite from EDP features, diffraction patterns with different zone axes were obtained from the single crystal region of the nitrided sample. Certainly, quite diffuse spots in the obtained EDPs were found no matter what the zones axes were (Figure 9). With a Au-calibrated camera constant ($L\lambda$) and within the accuracy of the TEM technique, the expanded austenite region retained the cubic structure and there was no obvious systematic lattice distortion. Typical diffraction patterns of $\langle 001 \rangle$ zone axes from a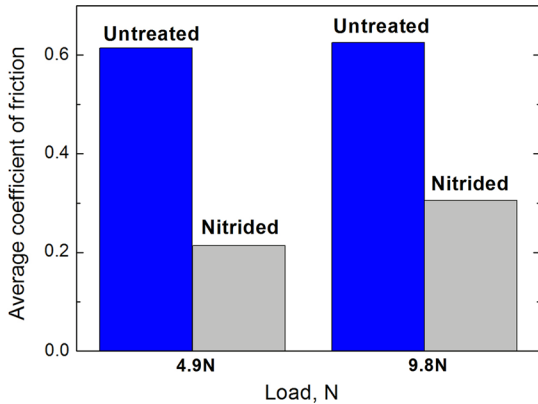 single-phase region of the nitrided sample and a single grain of the untreated sample, along with the boundary region of the nitrided sample, are shown in Figures 9(a) through (c). It can be distinctly observed that the spots from the expanded austenite show an obvious diffuse scattering effect in the form of broadening and tailing of the diffraction spots (Figure 9(b)). The lattice expansion was calculated from the (200) or (020) plane, compared with the identical zone axes of untreated austenite (Figure 9(a)). The measured lattice expansion was about 9.1 pct, equivalent with the lattice expansion (9.2 pct) from the XRD peak of (200) at a depth of 11.5 μm (from top surface), but smaller than the lattice expansion at the top surface of the nitrided sample (10.5 pct). In view of electron transparent foil of 100 to 200 nm, the information for TEM came from only the top 100 to 200 nm of the treated surface. Therefore, the inconsistency in the lattice expansions from XRD and TEM data was reasonable, because the residual compressive stresses causing the shift of XRD peaks had been released partly during TEM specimen preparation. The pattern of the $\langle 101 \rangle$ zone axis obtained from expanded austenite permitted determination of the ratio of (111)/(200) representing the distortion amount of the expanded austenite, as seen in Figure 9(d). Unfortunately, it was difficult to determine accurately the spacings of γ_{N1} from the EDP, and not to obtain the precise ratio due to the strong diffuse scattering effect on the diffraction spots. Fortunately, the angle between the crystal planes can be
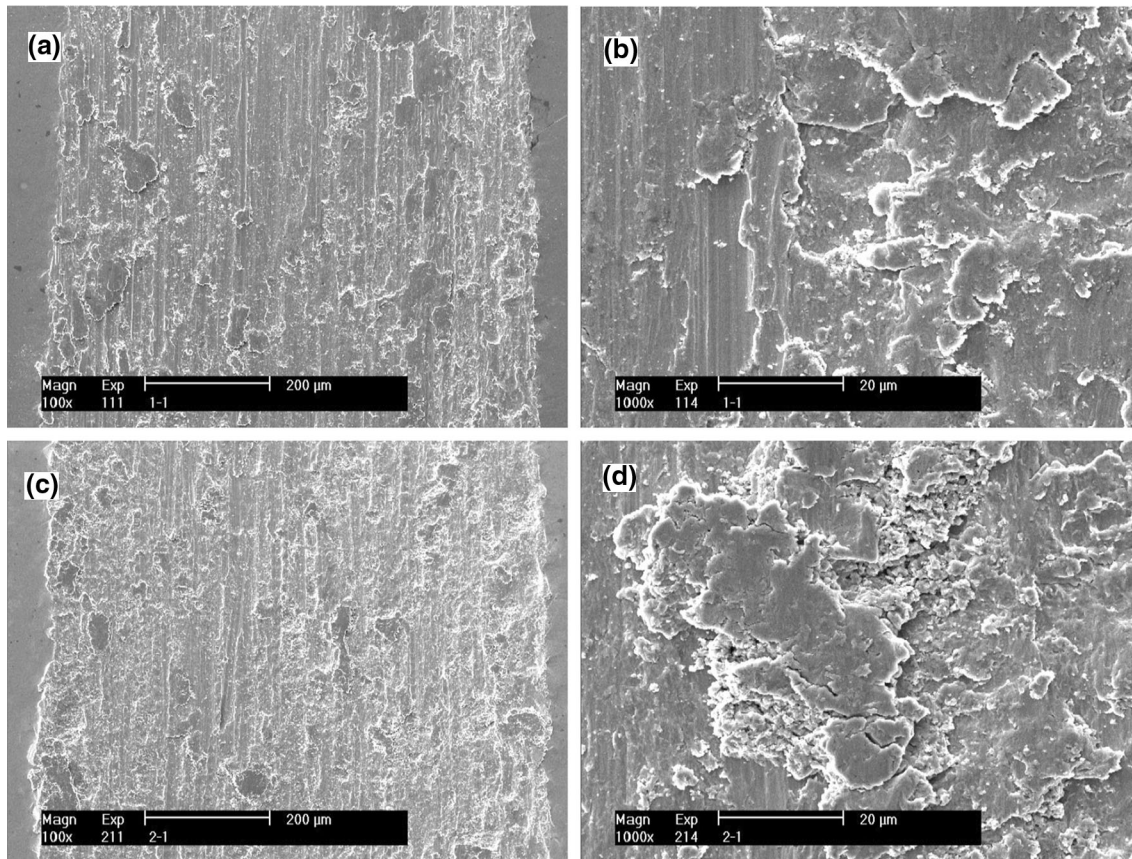

Fig. 11—Friction coefficients of nitrided and untreated samples.

Fig. 12—SEM observation on the wear track on the nitrided sample: (*a*) and (*b*) load of 5 N; (*c*) and (*d*) load of 10 N.
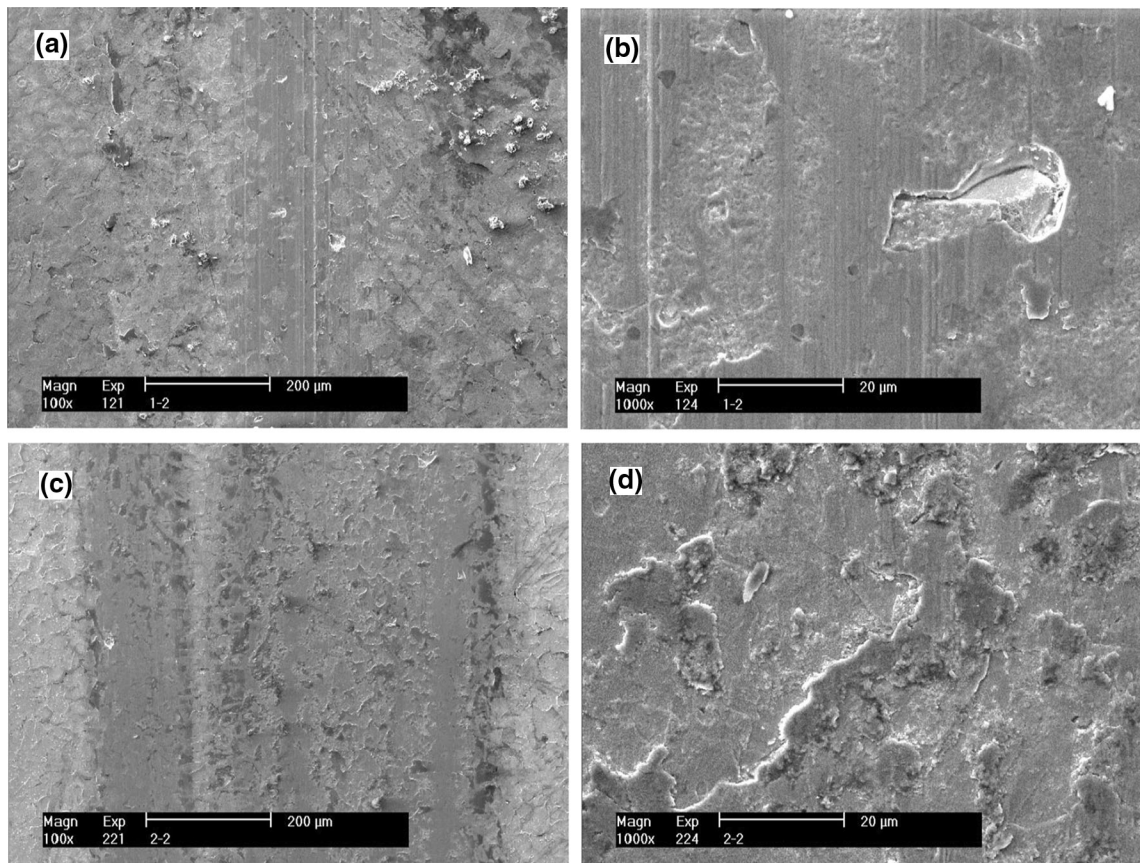
Fig. 13—SEM observation on the wear track on the nitrided sample: (*a*) and (*b*) load of 5 N; (*c*) and (*d*) load of 10 N.
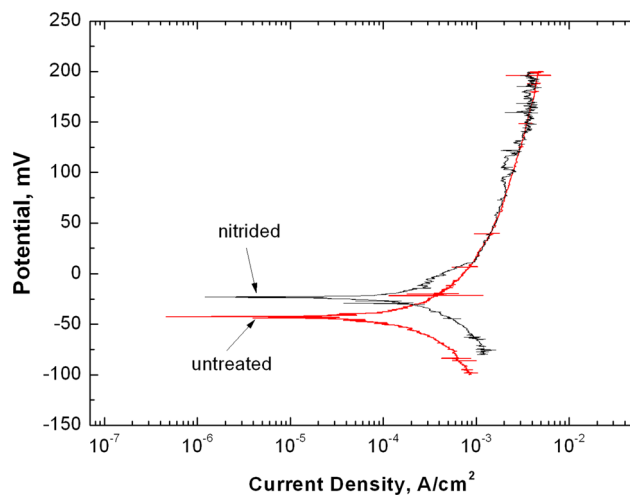

Fig. 14—Polarization curves of untreated and nitrided specimen in 3.5 pct NaCl solution.

measured accurately. The measured angle between $(11\bar{1})$ and (020) was 55 deg, approximate to the angle between both crystal planes of an ideal fcc structure, 54.7 deg. Additionally, the angle between the reflection planes in the EDP of the γ_{N1} in Figure 8 was well in agreement with the angle between the corresponding reflection planes of an ideal fcc structure. It was suggested that the expanded austenite γ_{N1} in the zones observed by TEM

still retained the cubic structure, and there was no tetragonal or triclinic distortion within the accuracy of TEM technology. Also, the absence of systematic lattice distortion relative to cubic in EDP further confirmed that the anomalous expansion in γ_{N1} was mainly attributed to the higher residual stress in the supersaturated nitrogen solution. It is well known that solid solutions with a short range of alloying element clusters or fine pre-precipitates coherent with the substrate, and short-range order of vacancies, usually exhibit diffused intensity maxima in their EDP, but the crystal defects (dislocations, stacking faults, *etc.*).[33] It was noted that the expanded austenite (γ_{N1}) region exhibited a much different microstructure from γ-austenite in the untreated sample. A good diffraction contrast in γ_{N1} cannot be observed, regardless of the foil thickness or grain orientation, compared with the untreated γ-austenite (Figure 8(b)). It seems that it has an amorphous phase contrast to some extent or a monotonous contrast.[34] The microstructural features were observed in the nitrided austenite and ferrite.[11] Most likely, these microstructural features revealed the initial stage of precipitation composed of the substitutional-interstitial solute-atom clusters. In consideration of a stronger affinity between Cr and N, the nitrogen content detectable in the γ_{N1} is higher than the equilibrium solubility limit of nitrogen in the austenite, and because of its better corrosion resistance, compared with the substrate, it was suggested that the γ_{N1} is a

supersaturated nitrogen austenite with Cr-N clusters or pairs in short ordering. The Cr-N pairs or clusters in the supersaturated solid solution (γ_{N1}) contributed to monotonous contrast and the corresponding diffuse effect of electron diffraction spots. Due to the low mobility of the Cr atoms compared with the interstitial N at the low treatment temperature, the formation of nitride in the nitriding process was mainly controlled by the diffusion of the metal atoms; therefore, the precipitation of chromium nitrides was effectively prevented within the grains at the low process temperature.

The discontinuous rings (the inset on the left in Figures 8 and 9(c)) from the grain boundary regions were identified as CrN and γ-Fe. It was suggested that the decomposition reaction of $\gamma_{N1} \rightarrow CrN + \gamma$-Fe occurred at the grain boundaries. Also, the orientations of both CrN and γ-Fe maintained cubic and cubic relationship; *i.e.*, the planes and the directions with identical Miller indices in both phases were parallel. The decomposition products of CrN + γ-Fe in the present superalloy were different from those in the nitrided 304 stainless steel, which were CrN + α-Fe.[13] This should be attributed to the higher Ni content in this superalloy, which is the element of strongly stabilizing the austenite. Although XRD peaks of nitride (CrN) were not detected and observable precipitates were also not revealed by OPM and SEM, fine CrN nitrides were found to precipitate at the boundaries by TEM. Cr, as a substitutional element, is practically immobile in the grain interiors, but can diffuse along the grain boundaries. Nitrogen, on the other hand, is extremely mobile. Because the growth of nitride is controlled by the long-range diffusion of substitutional elements, the formation and growth of nitride within the grains must be retarded by insufficient diffusion of the Cr atoms in low-temperature nitriding, as described previously. The grain boundary acts as a heterogeneous nucleation site and an enhanced diffusion path that effectively facilitates substitutional diffusion. Therefore, fine nitrides of CrN were found to precipitate preferentially along the austenite boundaries, and Cr-N clusters with short order were presented within the grains.

E. Hardness of Nitrided Layer

The surface hardness of the nitrided sample with various loads between 50 and 1000 g and the microhardness profiles on a cross section of nitrided sample were conducted. Figure 10(a) shows the variation of surface hardness (average value of five readings) with the load. This figure shows that the surface hardness decreased with increasing load due to more and more contributions of the softer substrate. The surface hardness of the nitrided sample was up to about 963 $HV_{0.05}$, about 4.5 times higher than that of the untreated sample. Certainly, the small indentation load would produce a larger measurement error. The microhardness profile is shown in Figure 10(b). The profile revealed a considerable hardness increase in the region of the γ_{N1} layer, followed by an obvious hardness decrease in the region of the γ_{N2} layer. The higher hardness level in the region of the γ_{N1} layer can be attributed to the

formation of the γ_{N1} phase with compressive residual stresses and microdistortion due to the high nitrogen content. The results suggested that nitriding on the superalloy would produce a case layer with a significantly higher microhardness than the untreated superalloy.

F. Tribological Behavior

Figure 11 shows the friction coefficients for both nitrided and untreated specimens. The friction coefficients of nitrided specimens were found to be 2 to 3 times lower than those of the untreated specimens. A decrease in the friction coefficient of the nitrided specimens was attributed to the remarkable increase in surface hardness of the nitrided specimens, which led to minimizing both deformation and adhesive friction of the asperities between the two contacted surfaces. For both nitrided and untreated specimens under dry sliding conditions, the friction coefficient increased slightly with increasing the contact load, because the higher load would increase the contact area between the two surfaces to adhere the asperities more strongly. The occurrence of more plastic and shear deformation of the asperities as well as adhesion between the two surfaces was responsible for the increase in the friction coefficient with increasing load.

The worn surfaces of untreated and nitrided specimens were observed by SEM. It was clear that the untreated superalloy suffered severe wear, as evidenced by the deep and wide wear tracks on the sample surfaces (Figure 12) and grooves, both on macro- and microscales present inside the track, in addition to the occurrence of a large amount of wear debris during the wear test. It was suggested that the wear of the untreated superalloy occurred by combined mechanisms of adhesion, abrasion, and plastic deformation. On the contrary, the worn surfaces of the nitrided specimens exhibited narrow and shallow wear tracks and no obvious signs of adhesive wear or plastic deformation in spite of local spalling due to the brittle layer (Figure 13). Nitriding has essentially changed the wear mechanism of the superalloy to mild microabrasion wear. The γ_N layer with higher hardness on the nitrided superalloy was beneficial to enhance the wear resistance of superalloy.

G. Corrosion Behavior

Figure 14 presents the anodic polarization behavior of untreated and nitrided specimens in 3.5 pct NaCl water solution. It can be seen that the polarization curves of both specimens do not show an evident passivation region. The nitrided samples exhibited a slightly higher corrosion potential, increasing from -0.40 V_{SCE} of the untreated specimen to -0.20 V_{SCE} of the nitrided specimen. Further, the corrosion current density of both specimens is of the same order ($\sim 2 \times 10^{-5}$ A/cm^2). It was suggested that the nitrided surface showed no adverse effect in the corrosion resistance, but a little improvement.

IV. CONCLUSIONS

1. The separate expanded austenite (γ_{N1} and γ_{N2}) layers with distinctly different nitrogen contents were formed on the nitrided Fe-base superalloy. The expanded austenite γ_{N2} was lying underneath the expanded austenite γ_{N1}, as detected by removal XRD and cross-sectional SEM and OPM observations. XRD results showed that large lattice expansion and lattice distortion occurred on γ_{N1}, but low expansion and less distortion took place on the γ_{N2}, relative to an ideal fcc structure. No obvious lattice distortion on the γ_{N1} was determined by calculating its EDP. Inconformity between the XRD and EDP results suggested that the high compressive residual stress in the γ_{N1} was mainly responsible for the occurrence of lattice distortion on the γ_{N1}.

2. The nitrogen concentration level in the γ_{N1} layer predicted from the lattice parameter of γ_{N1} by XRD was much higher than that from EDS evaluation, because the peak shift to the lower Bragg angle partially resulted from the higher residual stress in the γ_{N1}. The nitrogen concentration level in the γ_{N2} layer predicted from the lattice parameter of γ_{N2} by XRD was found to correlate well with the nitrogen concentration level from EDS evaluation

3. TEM observation revealed that the precipitation reaction of $\gamma_{N1} \rightarrow CrN + \gamma$ occurred along the grain boundaries as the enhanced diffusion paths of substitutional element Cr. The γ_{N1} exhibited monotonous contrast, probably reflective of fine pre-precipitation in the form of Cr-N clusters, whose EDP exhibited a strong diffuse scattering effect.

4. The nitrided superalloy surface exhibited high hardness and wear resistance. The nitrided superalloy surface showed no adverse effect in the corrosion resistance but a little improvement in the 3.5 pct NaCl water solution.

REFERENCES

1. X. Xu and Z. Yu: *Eng. Fail. Anal.*, 2009, vol. 16, pp. 1554–61.
2. M. Olzon-Dionysio, M. Campos, M. Kapp, S. De Souza, and S.D. De Souza: *Surf. Coat. Technol.*, 2010, vol. 204, pp. 3623–28.
3. D. Manova, C. Günther, A. Bergmann, S. Mändl, H. Heumann, and B. Rauschenbach: *Nucl. Instrum. Methods Phys. Res. B*, 2009, vol. 267, pp. 1536–39.
4. J. Wang, Y. Lin, J. Yan, D. Zen, Q. Zhang, R. Huang, and H. Fan: *Surf. Coat. Technol.*, 2012, vol. 206, pp. 3399–04.
5. Y. Sun, X.Y. Li, and T. Bell: *J. Mater. Sci.*, 1999, vol. 34, pp. 4793–02.
6. M.P. Fewell, D.R.G. Mitchell, J.M. Priest, K.T. Short, and G.A. Collins: *Surf. Coat. Technol.*, 2000, vol. 131, pp. 300–06.
7. T. Czerwiec, N. Renevier, and H. Michel: *Surf. Coat. Technol.*, 2000, vol. 131, pp. 267–77.
8. T. Christiansen and M.A.J. Somers: *Metall. Mater. Trans. A*, 2006, vol. 37A, pp. 675–82.
9. T. Christiansen and M.A.J. Somers: *Scripta Mater.*, 2004, vol. 50, pp. 35–37.
10. K. Marchev, M. Landis, R. Vallerio, C.V. Copper, and B.C. Giessen: *Surf. Coat. Technol.*, 1999, vols. 116–119, pp. 184–88.
11. Xu. Xiaolei, Yu. Zhiwei, Liying. Cui, Xinjun. Niu, and Tao. Cai: *Metall. Mater. Trans. A*, 2016, vol. 47A, pp. 801–10.
12. Matej. Fonović, Andreas. Leineweber, Odile. Robach, Eric.A. Jägle, and Eric.J. Mittemejer: *Metall. Mater. Trans. A*, 2015, vol. 46A, pp. 4115–31.
13. F.A.P. Fernandes, L.C. Casteletti, and J. Gallego: *J. Mater. Res. Technol.*, 2013, vol. 2, pp. 158–64.
14. C. Leroy, T. Czerwiec, C. Gabet, T. Belmonte, and H. Michel: *Surf. Coat. Technol.*, 2001, vols. 142–144, pp. 241–47.
15. V. Singh and E.I. Meletis: *Surf. Coat. Technol.*, 2006, vol. 201, pp. 1093–01.
16. S. Chollet, L. Pichon, J. Cormier, J.B. Villechaise, M. Drouet, A. Declemy, and C. Templier: *Surf. Coat. Technol.*, 2013, vol. 235, pp. 318–25.
17. D.L. Williamson, J.A. Davis, and P.J. Wilbur: *Surf. Coat. Technol.*, 1998, vols. 103–104, pp. 178–84.
18. F. Borgioli, A. Fossati, E. Galvanetto, T. Bacci, and G. Pradelli: *Surf. Coat. Technol.*, 2006, vol. 200, pp. 5505–31.
19. V. Raghavan: *J. Phase Equilibria*, 1997, vol. 18, pp. 158–72.
20. O. Öztürk and D.L. Williamson: *J. Appl. Phys.*, 1995, vol. 77, pp. 3839–50.
21. D.L. Williamson, O. Ozturk, R. Wei, and P.J. Wilbur: *Surf. Coat. Technol.*, 1994, vol. 65, pp. 15–23.
22. O. Celik, M. Baydogan, E. Atar, E.S. Kayali, and H. Cimenoglu: *Mater. Sci. Eng.*, 2013, vol. 565A, pp. 38–43.
23. T. Christiansen and M.A.J. Somers: *Metall. Mater. Trans. A*, 2009, vol. 40A, pp. 1791–98.
24. Y. Sun, X.Y. Li, and T. Bell: *J. Mater. Sci.*, 1999, vol. 34, pp. 4793–02.
25. E.I. Meletis, V. Singh, and J.C. Jiang: *J. Mater. Sci. Lett.*, 2002, vol. 21, pp. 1171–74.
26. X. Xu, L. Wang, Z. Yu, J. Qiang, and Z. Hei: *Metall. Mater. Trans. A*, 2000, vol. 31A, pp. 1193–99.
27. H. Kahn, G.M. Michal, F. Ernst, and A.H. Heuer: *Metall. Mater. Trans. A*, 2009, vol. 40A, pp. 1799–04.
28. M.A.J. Somers and E.J. Mittemeijer: *Metall. Mater. Trans. A*, 1990, vol. 21A, pp. 189–04.
29. B.E. Warren: *X-ray Diffraction*, Dover Publications Inc., New York, 1990, pp. 251–12.
30. B.D. Cullity and S.R. Stock: *X-ray Diffraction*, Prentice Hall, Upper Saddle River, NJ, 2001, pp. 284–91.
31. K. Marchev, C.V. Copper, J.T. Blucher, and B.C. Giessen: *Surf. Coat. Technol.*, 1998, vol. 99, pp. 225–28.
32. K. Marchev, R. Hidalgo, M. Landis, R. Vallerio, C.V. Copper, and B.C. Giessen: *Surf. Coat. Technol.*, 1999, vol. 112, pp. 67–70.
33. T. Christiansen and M.A.J. Somers: *Metall. Mater. Trans. A*, 2007, vol. 37A, pp. 675–82.
34. J.W. Edington: *Practice Electron Microscopy in Materials Science (Part II)*, The Macmillan Press, London, 1975, pp. 102–05.